

Three-dimensional DtN-FEM scattering analysis of Lamb and SH guided waves by a symmetric cavity defect in an isotropic infinite plate

Chen Yang^{a,b,*}, Junichi Nakaoka^b, Sohichi Hirose^b

^a*State Key Lab for Turbulence and Complex Systems, College of Engineering, Peking University, Beijing 100871, China*

^b*Tokyo Institute of Technology, 2-12-1-W8-22, O-okayama, Meguro, Tokyo, 152-8552, Japan*

Abstract

In this paper, a three-dimensional Dirichlet-to-Neumann (DtN) finite element method (FEM) is developed to analyze the scattering of Lamb and SH guided waves due to a symmetric cavity defect in an isotropic infinite plate. During the finite element analysis, it is necessary to determine the far-field DtN conditions at virtual boundaries where both displacements and tractions are unknown. In this study, firstly, the scattered waves at the virtual boundaries are represented by a superposition of guided waves with unknown scattered coefficients. Secondly, utilizing the mode orthogonality, the unknown tractions at virtual boundaries are expressed in terms of the unknown scattered displacements at virtual boundaries via scattered coefficients. Thirdly, this relationship at virtual boundaries can be finally assembled into the global DtN-FEM matrix to solve the problem. This method is simple and elegant, which has advantages on dimension reduction and needs no absorption medium or perfectly matched layer to suppress the reflected waves compared to traditional FEM. Furthermore, the reflection and transmission coefficients of each guided mode can be directly obtained without post-processing. This proposed DtN-FEM will be compared with boundary element method (BEM), and finally validated for several benchmark problems.

Keywords: 3D guided waves; 3D DtN-FEM; Virtual boundaries; Mode orthogonality

*Corresponding author

Email addresses: yangc@pku.edu.cn; yc@nuaa.edu.cn; yang.c.ag@m.titech.ac.jp (Chen Yang), junnakaoka0224@gmail.com (Junichi Nakaoka), shirose@cv.titech.ac.jp (Sohichi Hirose)

1. Introduction

Nondestructive testings demonstrate its absolute advantages and potential compared with other traditional destructive methods over the past few decades. As one of the nondestructive testings, the ultrasonic guided waves have naturally captured the attention of researchers. Although the conventional bulk wave detection technique has been widely used in many fields, the guided wave has lower preconditions, is more convenient to operate and needs to process fewer waveforms. These unique superiors cannot be replicated by bulk wave detection. Undoubtedly, the emergence of the guided wave technique has considerably reduced the cost of nondestructive testing.

Currently, many researchers have obtained huge achievements in quantitative non-destructive testing (QNDT) using ultrasonic guided waves [1, 2]. Wang proposed a prevalent method for shape and depth construction of plate, half space and layered semi-infinite space using whole reflection coefficients of SH waves [3, 4], Rayleigh Wave [5] and Love waves [6], respectively. In addition, Da et al. [7] utilize scattering coefficients of the torsional modes to reconstruct the defect shape in pipeline structures effectively. Consequently, it is enormously important to require a thorough understanding and accurate computation of forward scattering phenomenon, to acquire a database for QNDT research such as near-and-far field scattering data.

In the analysis of elastic guided wave scattering problems, two key aspects must be properly addressed and treated. First, due to the dispersive and multi-mode nature of guided and evanescent waves, the wavenumber and wave structures should be accurately determined by dispersion equations. Moreover, dispersion curves can be drawn analytically by solving transcendent equations with complex root-racking modulus-converging algorithm [8]. This information is useful for mode selection, as well as generation and reception of a single mode in non-destructive evaluation. Second, Lamb wave mode interaction with defects must be accurately determined, which is the focus of this paper. The complexity of mode conversion restrains an analytical approach to very simple geometries, and for more general cases, it requires valid numerical methods like FEM and BEM to obtain an accurate scattering wave-field. In our previous work, a modified BEM was proposed to solve the three-dimensional plate scattering problem [9], where only the interfaces and flaw boundaries need to be discretized. However, BEM needs to handle the singularity and compute the fundamental solution matrix numerically, and the final BEM matrix will be full-rank, which consume many storage and computing resources,

especially when simulating high frequency scattering problems.

Compared to BEM, FEM is particularly attractive for forward scattering analysis since FEM is more simple and popular, and the final global FEM matrix is sparse. For plate scattering computation, Koshiha [10] implemented the analysis of the scattering problem of Lamb waves in an elastic waveguide by FEM. Al-Nassar and Datta [11] used the Lamb wave to detect a normal rectangular strip weldment and obtained the guided waves' behavior at specific frequencies. A semi-analytical FEM proposed by Hayashi and Rose [12] was used to analyze the behavior of guided waves in plates and pipes. This method was soon applied to the field of flaw detection, for example, rail base [13, 14]. Gunawan and Hirose [15] provide a mode-exciting method to study the scattering phenomenon in an infinite plate. Moreover, the researchers also conducted related explorations in the processing approach of the scattering boundary. The orthogonality of guided wave modes was provided to solve the scattering problem in a plate [16]. Other researchers, such as Moreau [17], and Kubrusly [18, 19] try to apply this method to study relative objects.

The goal of this paper is to propose a FEM implemented in a bi-material plate to avoid the computation error caused by spurious reflected waves in 3-D scattering problems. During the finite element analysis, it is necessary to determine the far-field DtN conditions at virtual boundaries where both displacements and tractions are unknown. In this study, firstly, the scattered waves at the virtual boundaries are represented by a superposition of guided waves with unknown scattered coefficients. Secondly, utilizing the mode orthogonality, the unknown tractions at virtual boundaries are expressed in terms of the unknown scattered displacements at virtual boundaries via scattered coefficients. Thirdly, this relationship at virtual boundaries can be finally assembled into the global DtN-FEM matrix to solve the problem. This method is simple and elegant, which has advantages on dimension reduction and needs no absorption medium or perfectly matched layer to suppress the reflected waves compared to traditional FEM. Furthermore, the reflection and transmission coefficients of each guided mode can be directly obtained without post-processing. This proposed DtN-FEM will be compared with boundary element method (BEM), and finally validated for several benchmark problems. Finally, this proposed DtN-FEM will be applied into investigating the effect on different defect shapes.

2. Three-dimensional DtN FEM

2.1. General description of the problem

A three-dimensional elasto-dynamic problem in a infinite plate of homogeneous, isotropic, linearly elastic material with thickness $2h$ is considered as shown in Fig.1, referred to a Cartesian coordinate system such that $x_1 - x_2$ plane coincides with the mid-plane of the layer. The cavity flaw is symmetric about the mid-plane of the layer. The upper and lower surfaces of the plate and the flaw surface are stress-free. Let us consider an incident plane wave excited at the far-field interacting with a cavity of arbitrary shape and generating scattered waves. By virtue of linear superposition principle, the total field in the flawed structure can be considered as the superposition of the incident and scattered fields where the incident field is known and the scattered field is unknown. The aim of this paper is to simulate the unknown scattered field. In traditional FEM, extra absorbing materials or perfectly matched layered is utilized to absorb the spurious reflected waves in order to simulate the infinite domain. However, in this paper, the domain surrounded by the red dashed surface in Fig.1 is the actual simulation area. The key to the problem is how to deal with the far-field DtN conditions at the virtual boundary since displacements and tractions at the virtual boundary are both unknown.

2.2. Three-dimensional guided wave assumptions in an infinite isotropic plate

In the modeling of the problem using three-dimensional scattering theory, it is crucial to express the wave fields in an appropriate way. To analyze the scattered wave field in an infinite plate, it is a natural choice to adopt a cylindrical coordinate system (r, θ, z) to express the Lamb and SH wave modes. A way to represent the following Lamb and SH wave modes is to use a potential function as shown by Achenbach, and the general equation is as follows.

For a Lamb wave mode of order n , the displacements can be given as

$$u_r^n = \frac{1}{k_n} V_n(z) \frac{\partial \phi}{\partial r}(r, \theta), \quad u_\theta^n = \frac{1}{k_n r} V_n(z) \frac{\partial \phi}{\partial \theta}(r, \theta), \quad u_z^n = W_n(z) \phi(r, \theta). \quad (1)$$

where the scalar potential function $\phi(r, \theta)$ satisfies Helmholtz equation which in cylindrical coordinates reads

$$\frac{\partial^2 \phi}{\partial r^2} + \frac{1}{r} \frac{\partial \phi}{\partial r} + \frac{1}{r^2} \frac{\partial^2 \phi}{\partial \theta^2} + k_n^2 \phi = 0 \quad (2)$$

In Eq.1, k_n represents the wavenumber and $V_n(z)$ and $W_n(z)$ are the thickness coordinate dependent functions which differ for symmetric and anti-symmetric modes. For symmetric

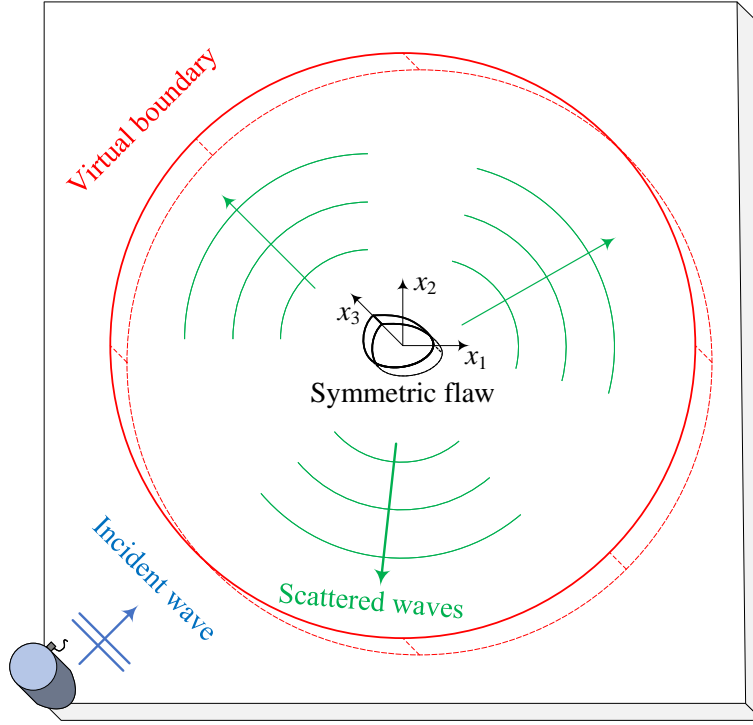


Figure 1: Boundary conditions along the horizontal direction.

Lamb wave, expressions for $V_n(z)$ and $W_n(z)$ are

$$V_n(z) = s_1 \cos(p_n z) + s_2 \cos(q_n z), \quad W_n(z) = s_3 \sin(p_n z) + s_4 \sin(q_n z), \quad (3)$$

where

$$s_1 = 2 \cos(q_n h), \quad s_2 = -\frac{k_n^2 - q_n^2}{k_n^2} \cos(p_n h), \quad (4)$$

$$s_3 = -\frac{2p_n}{k_n} \cos(q_n h), \quad s_4 = -\frac{k_n^2 - q_n^2}{q_n k_n} \cos(p_n h). \quad (5)$$

k_n is given by the root of the symmetric Rayleigh-Lamb equation

$$\frac{\tan(qh)}{\tan(ph)} = -\frac{4k^2 pq}{(q^2 - k^2)^2} \quad (6)$$

where $p^2 = k_L^2 - k_n^2$, $q^2 = k_T^2 - k_n^2$, and ω represents the angular frequency and k_L and k_T indicate the longitudinal and transverse wave velocities respectively.

SH wave modes can also be generated. Similarly, these modes can be expressed using a scalar potential function $\psi(r, \theta)$, as shown by

$$u_r^n = \frac{1}{l_n r} U_n(z) \frac{\partial \psi}{\partial \theta}(r, \theta), \quad u_\theta^n = -\frac{1}{l_n} U_n(z) \frac{\partial \psi}{\partial r}(r, \theta), \quad u_z^n = 0. \quad (7)$$

where the scalar potential $\psi(r, \theta)$ satisfies Helmholtz equation

$$\frac{\partial^2 \psi}{\partial r^2} + \frac{1}{r} \frac{\partial \psi}{\partial r} + \frac{1}{r^2} \frac{\partial^2 \psi}{\partial \theta^2} + l_n^2 \psi = 0 \quad (8)$$

and the thickness dependent functions $U_n(z)$ for symmetric SH modes are given by

$$U_n(z) = \cos\left(\frac{n\pi z}{2h}\right) \quad (n = 0, 2, 4, \dots) \quad (9)$$

The wavenumbers l_n for the SH modes are

$$l_n^2 = k_T^2 - \left(\frac{n\pi}{2h}\right)^2 \quad (10)$$

Next, we need to find proper expansions for the wave field. For this purpose, the solution of the scalar potentials $\phi(r, \theta)$ and $\psi(r, \theta)$ referred to reference for an outgoing wave are expressed as

$$\phi(r, \theta) = H_m(k_n r) e^{im\theta}, \quad \psi(r, \theta) = H_m(l_n r) e^{im\theta}. \quad (11)$$

respectively, where $H_m()$ indicate Hankel functions of the first kind.

Then the scattered displacement fields are obtained by expanding the wave fields in the allowed modes. For a fixed frequency, Eq.6 and Eq.10 have a finite number of real roots, corresponding to propagating modes, and an infinite number of complex roots, non-propagating modes. Thus, the scattered displacements and stresses at the far-field virtual boundary can be written as

$$\begin{aligned} u_r^{scat} &= \sum_{n=0}^{\infty} \sum_{m=-\infty}^{\infty} A_{mn} V_n(z) H'_m(k_n r) e^{im\theta} + \sum_{n=0,2,\dots}^{\infty} \sum_{m=-\infty}^{\infty} im B_{mn} \cos\left(\frac{n\pi z}{2h}\right) \frac{H_m(l_n r)}{l_n r} e^{im\theta}, \\ u_\theta^{scat} &= \sum_{n=0}^{\infty} \sum_{m=-\infty}^{\infty} im A_{mn} V_n(z) \frac{H_m(k_n r)}{k_n r} e^{im\theta} - \sum_{n=0,2,\dots}^{\infty} \sum_{m=-\infty}^{\infty} B_{mn} \cos\left(\frac{n\pi z}{2h}\right) H'_m(l_n r) e^{im\theta}, \\ u_z^{scat} &= \sum_{n=0}^{\infty} \sum_{m=-\infty}^{\infty} A_{mn} W_n(z) H_m(k_n r) e^{im\theta}. \end{aligned} \quad (12)$$

$$\begin{aligned}
\sigma_r^{scat} &= \sum_{n=0}^{\infty} \sum_{m=-\infty}^{\infty} A_{mn} \left[\sum_{rr}^n(z) H_m(k_n r) - \tilde{\sum}_{rr}^n(z) \left(\frac{1}{r} H'_m(k_n r) - \frac{m^2}{k_n r^2} H_m(k_n r) \right) \right] e^{im\theta} \\
&+ \sum_{n=0,2,\dots}^{\infty} \sum_{m=-\infty}^{\infty} im B_{mn} \mu \cos\left(\frac{n\pi z}{2h}\right) \left(\frac{2}{r} H'_m(l_n r) - \frac{2}{l_n r^2} H_m(l_n r) \right) e^{im\theta}, \\
\tau_{r\theta}^{scat} &= \sum_{n=0}^{\infty} \sum_{m=-\infty}^{\infty} im A_{mn} \sum_{r\theta}^n(z) \left(\frac{1}{r} H'_m(k_n r) - \frac{1}{k_n r^2} H_m(k_n r) \right) e^{im\theta} \\
&+ \sum_{n=0,2,\dots}^{\infty} \sum_{m=-\infty}^{\infty} B_{mn} \mu \cos\left(\frac{n\pi z}{2h}\right) \left[\frac{2}{r} H'_m(l_n r) + \left(l_n - \frac{2m^2}{l_n r^2} \right) H_m(l_n r) \right] e^{im\theta} \\
\tau_{rz}^{scat} &= - \sum_{n=0}^{\infty} \sum_{m=-\infty}^{\infty} A_{mn} \sum_{rz}^n(z) H'_m(k_n r) e^{im\theta} \\
&- \sum_{n=2,4,\dots}^{\infty} \sum_{m=-\infty}^{\infty} im B_{mn} \mu \frac{n\pi}{2h} \sin\left(\frac{n\pi z}{2h}\right) \frac{1}{l_n r} H_m(l_n r) e^{im\theta}.
\end{aligned} \tag{13}$$

respectively, where A_{mn} and B_{mn} account for the expansion coefficients which have to be found in order to obtain the scattered field, μ is the second Lamé constant and

$$\begin{aligned}
\sum_{rr}^n(z) &= \mu [s_5 \cos(p_n z) + s_6 \cos(q_n z)], \\
\tilde{\sum}_{rr}^n(z) &= \sum_{r\theta}^n(z) = \mu [s_7 \cos(p_n z) + s_8 \cos(q_n z)], \\
\sum_{rz}^n(z) &= \mu [s_9 \sin(p_n z) + s_{10} \sin(q_n z)],
\end{aligned} \tag{14}$$

$$s_5 = \frac{2(2p_n^2 - k_n^2 - q_n^2)}{k_n} \cos(q_n h), \quad s_6 = \frac{2(k_n^2 - q_n^2)}{k_n} \cos(p_n h), \quad s_7 = 4 \cos(q_n h), \tag{15}$$

$$s_8 = -\frac{2(k_n^2 - q_n^2)}{k_n^2} \cos(q_n h), \quad s_9 = 4p_n \cos(q_n h), \quad s_{10} = \frac{(k_n^2 - q_n^2)^2}{q_n k_n^2} \cos(p_n h). \tag{16}$$

In actual numerical computations, the summation for the angular dependence m and mode n are truncated at $|m| = M$ and $n = N$ respectively.

Next, the general equation for the displacement in the incident field is considered. Since the incident field is given by a symmetric plane Lamb wave and only the case of zero mode is considered, the expression for the scalar potential is expressed by the equation below.

$$\phi^{\text{inc}} = e^{ik_0 x} = e^{ik_0 r \cos \theta} = \sum_{m=-\infty}^{\infty} i^m J_m(k_0 r) e^{im\theta} \tag{17}$$

where $J_m()$ is a Bessel function of the first kind. The incident displacements and stresses can

be written as

$$\begin{aligned}
u_r^{\text{inc}} &= \sum_{m=-\infty}^{\infty} i^m V_0(z) J'_m(k_0 r) e^{im\theta}, \\
u_\theta^{\text{inc}} &= \sum_{m=-\infty}^{\infty} m i^{m+1} V_0(z) \frac{J_m(k_0 r)}{k_0 r} e^{im\theta}, \\
u_z^{\text{inc}} &= \sum_{m=-\infty}^{\infty} i^m W_0(z) J_m(k_0 r) e^{im\theta}.
\end{aligned} \tag{18}$$

$$\begin{aligned}
\sigma_r^{\text{inc}} &= \sum_{m=-\infty}^{\infty} i^m \left[\sum_{rr}^0(z) J_m(k_0 r) - \tilde{\sum}_{rr}^0(z) \left(\frac{1}{r} J'_m(k_0 r) - \frac{m^2}{k_0 r^2} J_m(k_0 r) \right) \right] e^{im\theta}, \\
\tau_{r\theta}^{\text{inc}} &= \sum_{m=-\infty}^{\infty} i^{m+1} m \sum_{r\theta}^0(z) \left(\frac{1}{r} J'_m(k_0 r) - \frac{1}{k_0 r^2} J_m(k_0 r) \right) e^{im\theta}, \\
\tau_{rz}^{\text{inc}} &= - \sum_{m=-\infty}^{\infty} \sum_{rz}^0(z) J_m(k_0 r) e^{im\theta}.
\end{aligned} \tag{19}$$

2.3. Far-field DtN conditions at the virtual boundaries

In order to get the relationship between displacements and tractions at the virtual boundary, the mode orthogonality should be utilized firstly. In simplifying the equations, this study focuses on the orthogonality of each term in the right-hand side of Eq.12 and Eq.13 and proceeds by multiplying each projection function, and the procedure is described below. Firstly, the projection function in the direction of θ is $e^{-im'\theta}$ ($-M \ll m' \ll M$) and the orthogonality of the projection function is

$$\int_{-\pi}^{\pi} e^{im\theta} e^{-im'\theta} d\theta = \begin{cases} 2\pi & (m = m') \\ 0 & (m \neq m') \end{cases} \tag{20}$$

Next, when considering the projection function in the z -direction, there is no clear function for the term of the Lamb mode. However, for the SH mode terms, only $\cos(n\pi z/2h)$ for u_r^{scat} and u_θ^{scat} , and $\sin(n\pi z/2h)$ for u_z^{scat} can be found to be z -dependent functions. Therefore, the projection function in the z direction is

$$\int_{-h}^h \cos\left(\frac{n\pi z}{2h}\right) \cdot \cos\left(\frac{n'\pi z}{2h}\right) dz = \begin{cases} 2h & (n = n' = 0) \\ h & (n = n' \neq 0) \\ 0 & (n \neq n') \end{cases}, \tag{21}$$

$$\int_{-h}^h \sin\left(\frac{n\pi z}{2h}\right) \cdot \sin\left(\frac{n'\pi z}{2h}\right) d\theta = \begin{cases} 0 & (n = n' = 0) \\ h & (n = n' \neq 0) \\ 0 & (n \neq n') \end{cases} \quad (22)$$

Therefore, the z -dependent orthogonal functions for the expressions u_r^{sca} and u_θ^{sca} are $\cos(n'\pi z/2h)$ where $n' = 0, 2, 4, \dots, N$ and the z -dependent orthogonal functions for the expression u_z^{sca} are $\sin(n'\pi z/2h)$ where $n' = 2, 4, \dots, N$. Thus, the orthogonal projection functions for u_r^{sca} and u_θ^{sca} can be defined as

$$\frac{1}{2\pi\mu} \cos\left(\frac{\acute{n}\pi z}{2h}\right) e^{-i\acute{m}\theta} \quad \acute{n} = 0, 2, \dots, N \quad (23)$$

and the orthogonal projection functions for u_z^{sca} are selected as

$$\frac{1}{2\pi\mu} \sin\left(\frac{\acute{n}'\pi z}{2h}\right) e^{-i\acute{m}'\theta} \quad \acute{n}' = 2, 4, \dots, N \quad (24)$$

Firstly, the equation u_r^{sca} is transformed. Multiplying both sides of Eq.12 by Eq.23 yields

$$\begin{aligned} & \frac{1}{2\pi\mu} \cos\left(\frac{\acute{n}'\pi z}{2h}\right) e^{-i\acute{m}'\theta} u_r^{\text{scat}} \\ &= \sum_{n=0}^N \sum_{m=-M}^M \frac{1}{2\pi\mu} \cos\left(\frac{\acute{n}'\pi z}{2h}\right) e^{-i\acute{m}'\theta} A_{mn} V_n(z) H'_m(k_n r) e^{im\theta} \\ &+ \sum_{n=0,2,\dots}^N \sum_{m=-M}^M \frac{1}{2\pi\mu} \cos\left(\frac{\acute{n}'\pi z}{2h}\right) e^{-i\acute{m}'\theta} i m B_{mn} \cos\left(\frac{n\pi z}{2h}\right) \frac{H_m(l_n r)}{l_n r} e^{im\theta} \end{aligned} \quad (25)$$

Applying a surface integral about the virtual surface of radius a to both sides of the above equation, we can achieve

$$\begin{aligned} & \int_S \frac{1}{2\pi\mu} \cos\left(\frac{\acute{n}\pi z}{2h}\right) e^{-i\acute{m}\theta} u_r^{\text{sca}} dS \\ &= \sum_{n=0}^N \sum_{m=-M}^M \int_{-\pi}^{\pi} \int_{-h}^h \frac{1}{2\pi\mu} \cos\left(\frac{\acute{n}'\pi z}{2h}\right) V_n(z) H'_m(k_n a) e^{i(m-m')\theta} A_{mn} a d\theta dz \\ &+ \sum_{n=0,2,\dots}^N \sum_{m=-M}^M \int_{-\pi}^{\pi} \int_{-h}^h \frac{i m}{2\pi\mu} \cos\left(\frac{\acute{n}'\pi z}{2h}\right) \cos\left(\frac{n\pi z}{2h}\right) \frac{H_m(l_n a)}{l_n a} e^{i(m-m')\theta} B_{mn} a d\theta dz \end{aligned} \quad (26)$$

$$\Leftrightarrow \int_S \frac{1}{2\pi\mu} \cos\left(\frac{n'\pi z}{2h}\right) e^{-im'\theta} u_r^{\text{sca}} dS = \sum_{n=0}^N \left[\frac{a}{\mu} H'_{m'}(k_n a) \int_{-h}^h \cos\left(\frac{n'\pi z}{2h}\right) V_n(z) dz \right] A_{m'n} + \left[\frac{im' H_{m'}(l_n' a)}{\mu l_n'} \right] \quad (27)$$

Secondly, the equation u_θ^{sca} is transformed. Multiplying both sides of Eq.12 by Eq.23 yields

$$\begin{aligned} & \frac{1}{2\pi\mu} \cos\left(\frac{n'\pi z}{2h}\right) e^{-im'\theta} u_\theta^{\text{sca}} \\ &= \sum_{n=0}^N \sum_{m=-M}^M \frac{1}{2\pi\mu} \cos\left(\frac{n'\pi z}{2h}\right) e^{-im'\theta} i m A_{mn} V_n(z) \frac{H_m(k_n r)}{k_n r} e^{im\theta} \\ & \quad - \sum_{n=0,2,\dots}^N \sum_{m=-M}^M \frac{1}{2\pi\mu} \cos\left(\frac{n'\pi z}{2h}\right) e^{-im'\theta} B_{mn} \cos\left(\frac{n\pi z}{2h}\right) H'_m(l_n r) e^{im\theta} \end{aligned} \quad (28)$$

Applying the same surface integral about the virtual surface of radius a to both sides of the above equation, we can achieve

$$\begin{aligned} & \int_S \frac{1}{2\pi\mu} \cos\left(\frac{n'\pi z}{2h}\right) e^{-im'\theta} u_\theta^{\text{sca}} dS \\ &= \sum_{n=0}^N \sum_{m=-M}^M \int_{-\pi}^{\pi} \int_{-h}^h \frac{im}{2\pi\mu} \cos\left(\frac{n'\pi z}{2h}\right) V_n(z) \frac{H_m(k_n a)}{k_n a} e^{i(m-m')\theta} A_{mn} a d\theta dz \\ & \quad - \sum_{n=0,2,\dots}^N \sum_{m=-M}^M \int_{-\pi}^{\pi} \int_{-h}^h \frac{1}{2\pi\mu} \cos\left(\frac{n'\pi z}{2h}\right) \cos\left(\frac{n\pi z}{2h}\right) H'_m(l_n a) e^{i(m-m')\theta} B_{mn} a d\theta dz \\ & \Leftrightarrow \int_S \frac{1}{2\pi\mu} \cos\left(\frac{n'\pi z}{2h}\right) e^{-im'\theta} u_\theta^{\text{sca}} dS \\ & \quad = \sum_{n=0}^N \left[\frac{im' H_{m'}(k_n a)}{\mu k_n} \int_{-h}^h \cos\left(\frac{n'\pi z}{2h}\right) V_n(z) dz \right] A_{m'n} \\ & \quad \quad - \left[\frac{a H'_{m'}(l_n' a)}{\mu} I_{nn'}^S \right] B_{m'n'} \left(n' = 0, 2, \dots, N \right). \end{aligned} \quad (29)$$

Finally, the equation u_z^{sca} is transformed. Multiplying both sides of Eq.12 by Eq.24 yields

$$\begin{aligned} & \frac{1}{2\pi\mu} \sin\left(\frac{n'\pi z}{2h}\right) e^{-im'\theta} u_z^{\text{sca}} \\ &= \sum_{n=0}^N \sum_{m=-M}^M \frac{1}{2\pi\mu} \sin\left(\frac{n'\pi z}{2h}\right) e^{-im'\theta} A_{mn} W_n(z) H_m(k_n r) e^{im\theta}. \end{aligned} \quad (31)$$

Applying the same surface integral about the virtual surface of radius a to both sides of the

above equation, we can achieve

$$\begin{aligned} & \int_S \frac{1}{2\pi\mu} \sin\left(\frac{n'\pi z}{2h}\right) e^{-im'\theta} u_z^{\text{sca}} dS \\ &= \sum_{n=0}^N \sum_{m=-M}^M \int_{-\pi}^{\pi} \int_{-h}^h \frac{1}{2\pi\mu} \sin\left(\frac{n'\pi z}{2h}\right) W_n(z) H_m(k_n a) e^{i(m-m')\theta} A_{mn} a d\theta dz \end{aligned} \quad (32)$$

$$\begin{aligned} & \Leftrightarrow \int_S \frac{1}{2\pi\mu} \sin\left(\frac{n'\pi z}{2h}\right) e^{-im'\theta} u_z^{\text{sca}} dS \\ &= \sum_{n=0}^N \left[\frac{a H_{m'}(k_n a)}{\mu} \int_{-h}^h \sin\left(\frac{n'\pi z}{2h}\right) W_n(z) dz \right] A_{m'n} \quad (n' = 2, 4, \dots, N) \end{aligned} \quad (33)$$

The above orthogonality technique allowed A_{mn} and B_{mn} to be obtained. In the above equations, m can be determined to any value m' and A_{mn} , B_{mn} can be considered separately for each m' . Eq.27, Eq.30 and Eq.33 can be rewritten into the matrix form as follows

$$\begin{bmatrix} \int_S \frac{1}{2\pi\mu} \cos\left(\frac{0\cdot\pi z}{2h}\right) e^{-im'\theta} u_r^{\text{sca}} dS \\ \vdots \\ \int_S \frac{1}{2\pi\mu} \cos\left(\frac{N\pi z}{2h}\right) e^{-im'\theta} u_r^{\text{sca}} dS \\ \int_S \frac{1}{2\pi\mu} \cos\left(\frac{0\cdot\pi z}{2h}\right) e^{-im'\theta} u_\theta^{\text{sca}} dS \\ \vdots \\ \int_S \frac{1}{2\pi\mu} \cos\left(\frac{N\pi z}{2h}\right) e^{-im'\theta} u_\theta^{\text{sca}} dS \\ \int_S \frac{1}{2\pi\mu} \sin\left(\frac{2\pi z}{2h}\right) e^{-im'\theta} u_z^{\text{sca}} dS \\ \vdots \\ \int_S \frac{1}{2\pi\mu} \sin\left(\frac{N\pi z}{2h}\right) e^{-im'\theta} u_z^{\text{sca}} dS \end{bmatrix} = \left[\bar{A} \bar{B}_{m'} \right]_{\left(\frac{3}{2}N+3\right) \times (N+2)} \begin{bmatrix} A_{m'0} \\ A_{m'1} \\ \vdots \\ A_{m'N} \\ B_{m'0} \\ B_{m'2} \\ \vdots \\ B_{m'N} \end{bmatrix}. \quad (34)$$

where

$$\left[\bar{A} \bar{B}_{m'} \right] = \left[\bar{A}_{m'} \quad \bar{B}_{m'} \right], \quad (35)$$

$$\begin{aligned}
& \left[\bar{A}_{m'} \right]_{\left(\frac{3}{2}N+3\right) \times \left(\frac{1}{2}N+1\right)} = \\
& \left[\begin{array}{ccc}
\frac{a}{\mu} H'_{m'}(k_0 a) \int_{-h}^h \cos\left(\frac{0 \cdot \pi z}{2h}\right) V_0(z) dz & \cdots & \frac{a}{\mu} H'_{m'}(k_N a) \int_{-h}^h \cos\left(\frac{0 \cdot \pi z}{2h}\right) V_N(z) dz \\
\vdots & \ddots & \vdots \\
\frac{a}{\mu} H'_{m'}(k_0 a) \int_{-h}^h \cos\left(\frac{N \pi z}{2h}\right) V_0(z) dz & \cdots & \frac{a}{\mu} H'_{m'}(k_N a) \int_{-h}^h \cos\left(\frac{N \pi z}{2h}\right) V_N(z) dz \\
\frac{im' H'_{m'}(k_0 a)}{\mu k_0} \int_{-h}^h \cos\left(\frac{0 \cdot \pi z}{2h}\right) V_0(z) dz & \cdots & \frac{im' H'_{m'}(k_N a)}{\mu k_n} \int_{-h}^h \cos\left(\frac{0 \cdot \pi z}{2h}\right) V_N(z) dz \\
\vdots & \ddots & \vdots \\
\frac{im' H'_{m'}(k_0 a)}{\mu k_0} \int_{-h}^h \cos\left(\frac{N \pi z}{2h}\right) V_0(z) dz & \cdots & \frac{im' H'_{m'}(k_N a)}{\mu k_N} \int_{-h}^h \cos\left(\frac{N \pi z}{2h}\right) V_N(z) dz \\
\frac{a H'_{m'}(k_0 a)}{\mu} \int_{-h}^h \sin\left(\frac{2 \pi z}{2h}\right) W_0(z) dz & \cdots & \frac{a H'_{m'}(k_N a)}{\mu} \int_{-h}^h \sin\left(\frac{2 \pi z}{2h}\right) W_N(z) dz \\
\vdots & \ddots & \vdots \\
\frac{a H'_{m'}(k_0 a)}{\mu} \int_{-h}^h \sin\left(\frac{N \pi z}{2h}\right) W_0(z) dz & \cdots & \frac{a H'_{m'}(k_N a)}{\mu} \int_{-h}^h \sin\left(\frac{N \pi z}{2h}\right) W_N(z) dz
\end{array} \right], \quad (36)
\end{aligned}$$

$$\begin{aligned}
& \left[\bar{B}_{m'} \right]_{\left(\frac{3}{2}N+3\right) \times \left(\frac{1}{2}N+1\right)} = \\
& \left[\begin{array}{cccc}
\frac{im' H'_{m'}(l_0 a)}{\mu l_0} I_{00}^S & 0 & \cdots & 0 \\
0 & \frac{im' H'_{m'}(l_2 a)}{\mu l_2} I_{22}^S & \cdots & 0 \\
\vdots & \vdots & \ddots & \vdots \\
0 & 0 & \cdots & \frac{im' H'_{m'}(l_N a)}{\mu l_n} I_{NN}^S \\
-\frac{a H'_{m'}(l_0 a)}{\mu} I_{00}^S & 0 & \cdots & 0 \\
0 & -\frac{a H'_{m'}(l_2 a)}{\mu} I_{22}^S & \cdots & 0 \\
\vdots & \vdots & \ddots & \vdots \\
0 & 0 & \cdots & -\frac{a H'_{m'}(l_n a)}{\mu} I_{NN}^S \\
0 & 0 & \cdots & 0 \\
\vdots & \vdots & \ddots & \vdots \\
0 & 0 & \cdots & 0
\end{array} \right]. \quad (37)
\end{aligned}$$

The actual calculation requires the left-hand side of Eq.34 to be calculated in discretised form, and the process is explained here. The integral on the left-hand side of Eq.34 is a surface integral, so it needs to be discretised using a two-dimensional shape function. Here, a four-node

quadrilateral element (Q4) is adopted. Then, we can get

$$\begin{aligned}
& \int_S \frac{1}{2\pi\mu} \cos\left(\frac{n'\pi z}{2h}\right) e^{-im'\theta} u_r^{\text{sca}} dS \\
&= \int_S \frac{1}{2\pi\mu} \cos\left(\frac{n'\pi z}{2h}\right) e^{-im'\theta} N_J u_r^{\text{sca}} dS \\
&= \left\{ \int_S \frac{1}{2\pi\mu} \cos\left(\frac{n'\pi z}{2h}\right) e^{-im'\theta} N_J dS \right\} u_r^{\text{sca}}{}_J \\
&= \left\{ \int_S \frac{1}{2\pi\mu} \cos\left(\frac{n'\pi z}{2h}\right) e^{-im'\theta} N_J dS \right\} \left(u_x^{\text{sca}}{}_J \cos\theta + u_y^{\text{sca}}{}_J \sin\theta \right),
\end{aligned} \tag{38}$$

$$\begin{aligned}
& \int_S \frac{1}{2\pi\mu} \cos\left(\frac{n'\pi z}{2h}\right) e^{-im'\theta} u_\theta^{\text{sca}} dS \\
&= \int_S \frac{1}{2\pi\mu} \cos\left(\frac{n'\pi z}{2h}\right) e^{-im'\theta} N_J u_\theta^{\text{sca}} dS \\
&= \left\{ \int_S \frac{1}{2\pi\mu} \cos\left(\frac{n'\pi z}{2h}\right) e^{-im'\theta} N_J dS \right\} u_\theta^{\text{sca}}{}_J \\
&= \left\{ \int_S \frac{1}{2\pi\mu} \cos\left(\frac{n'\pi z}{2h}\right) e^{-im'\theta} N_J dS \right\} \left(-u_x^{\text{sca}}{}_J \cos\theta + u_y^{\text{sca}}{}_J \sin\theta \right),
\end{aligned} \tag{39}$$

$$\begin{aligned}
& \int_S \frac{1}{2\pi\mu} \sin\left(\frac{n'\pi z}{2h}\right) e^{-im'\theta} u_z^{\text{sca}} dS \\
&= \int_S \frac{1}{2\pi\mu} \sin\left(\frac{n'\pi z}{2h}\right) e^{-im'\theta} N_J u_z^{\text{sca}} dS \\
&= \left\{ \int_S \frac{1}{2\pi\mu} \sin\left(\frac{n'\pi z}{2h}\right) e^{-im'\theta} N_J dS \right\} u_z^{\text{sca}}{}_J.
\end{aligned} \tag{40}$$

where J is the local node number. Projecting the integral value on the local node J in Eq.38, Eq.39 and Eq.40 onto the global node p , we get

$$\begin{aligned}
& \int_S \frac{1}{2\pi\mu} \cos\left(\frac{n'\pi z}{2h}\right) e^{-im'\theta} N_J dS \cdot \cos\theta \rightarrow D_{m'n'}^r{}^{x_p} = D_{m'n'}^r{}^p \cos\theta_p, \\
& \int_S \frac{1}{2\pi\mu} \cos\left(\frac{n'\pi z}{2h}\right) e^{-im'\theta} N_J dS \cdot \sin\theta \rightarrow D_{m'n'}^r{}^{y_p} = D_{m'n'}^r{}^p \sin\theta_p, \\
& \int_S \frac{1}{2\pi\mu} \cos\left(\frac{n'\pi z}{2h}\right) e^{-im'\theta} N_J dS \cdot (-\cos\theta) \rightarrow D_{m'n'}^\theta{}^{x_p} = -D_{m'n'}^\theta{}^p \sin\theta_p, \\
& \int_S \frac{1}{2\pi\mu} \cos\left(\frac{n'\pi z}{2h}\right) e^{-im'\theta} N_J dS \cdot \sin\theta \rightarrow D_{m'n'}^\theta{}^{y_p} = D_{m'n'}^\theta{}^p \cos\theta_p, \\
& \int_S \frac{1}{2\pi\mu} \sin\left(\frac{n'\pi z}{2h}\right) e^{-im'\theta} N_J dS \rightarrow D_{m'n'}^z{}^{z_p} = D_{m'n'}^z{}^p.
\end{aligned} \tag{41}$$

Then the left-hand side of Eq.34 can be rewritten as

$$[D_{m'}]_{(\frac{3}{2}N+2)\times 3p} \cdot [u_{xyz}^{sca}]_{3p\times 1} = \begin{bmatrix} \bar{A} \\ \bar{B} \end{bmatrix}_{(\frac{3}{2}N+2)\times(\frac{3}{2}N+2)} \cdot \begin{bmatrix} A_{m'} \\ B_{m'} \end{bmatrix}_{(\frac{3}{2}N+2)\times 1} \quad (42)$$

where

$$[D_{m'}]_{(\frac{3}{2}N+2)\times 3p} = \begin{bmatrix} D_{m'0}^r \ x_1 & D_{m'0}^r \ y_1 & 0 & \cdots & D_{m'0}^r \ x_p & D_{m'0}^r \ y_p & 0 \\ \vdots & \vdots & \vdots & \ddots & \vdots & \vdots & \vdots \\ D_{m'N}^r \ x_1 & D_{m'N}^r \ y_1 & 0 & \cdots & D_{m'N}^r \ x_p & D_{m'N}^r \ y_p & 0 \\ D_{m'0}^\theta \ x_1 & D_{m'0}^\theta \ y_1 & 0 & \cdots & D_{m'0}^\theta \ x_p & D_{m'0}^\theta \ y_p & 0 \\ \vdots & \vdots & \vdots & \ddots & \vdots & \vdots & \vdots \\ D_{m'N}^\theta \ x_1 & D_{m'N}^\theta \ y_1 & 0 & \cdots & D_{m'N}^\theta \ x_p & D_{m'N}^\theta \ y_p & 0 \\ 0 & 0 & D_{m'2}^z \ z_1 & \cdots & 0 & 0 & D_{m'2}^z \ z_p \\ \vdots & \vdots & \vdots & \ddots & \vdots & \vdots & \vdots \\ 0 & 0 & D_{m'N}^z \ z_1 & \cdots & 0 & 0 & D_{m'N}^z \ z_p \end{bmatrix}, \quad (43)$$

$$[u_{xyz}^{sca}]_{3p\times 1} = \begin{bmatrix} u_{x_1}^{sca} \\ u_{y_1}^{sca} \\ u_{z_1}^{sca} \\ u_{x_2}^{sca} \\ \vdots \\ u_{z_p}^{sca} \end{bmatrix}. \quad (44)$$

According to Eq.42, the unknown scattered coefficients for each m' can be expressed as

$$\begin{bmatrix} A_{m'} \\ B_{m'} \end{bmatrix}_{(\frac{3}{2}N+2)\times 1} = \begin{bmatrix} \bar{A} \\ \bar{B} \end{bmatrix}_{(\frac{3}{2}N+2)\times(\frac{3}{2}N+2)}^{-1} \cdot [D_{m'}]_{(\frac{3}{2}N+2)\times 3p} \cdot [u_{xyz}^{sca}]_{3p\times 1} \quad (45)$$

Next, the relationship between the unknown scattered coefficients and the node stresses at the virtual boundary will be established. Due to Eq.13, the stress expressions at the virtual

boundary can be rewritten as

$$\begin{aligned}
\sigma_{rr}^{scat} &= \sum_{m'=-M}^M \begin{bmatrix} E_{rr}^{m'}(\theta, z) \\ B_{m'} \end{bmatrix} \begin{bmatrix} A_{m'} \\ B_{m'} \end{bmatrix} = \sum_{m'=-M}^M \begin{bmatrix} E_{rr}^{m'}(\theta, z) \\ B_{m'} \end{bmatrix} \begin{bmatrix} \bar{A}B_{m'} \\ \bar{B} \end{bmatrix}^{-1} [D_{m'}] [u_{xyz}^{sca}], \\
\sigma_{r\theta}^{scat} &= \sum_{m'=-M}^M \begin{bmatrix} E_{r\theta}^{m'}(\theta, z) \\ B_{m'} \end{bmatrix} \begin{bmatrix} A_{m'} \\ B_{m'} \end{bmatrix} = \sum_{m'=-M}^M \begin{bmatrix} E_{r\theta}^{m'}(\theta, z) \\ B_{m'} \end{bmatrix} \begin{bmatrix} \bar{A}B_{m'} \\ \bar{B} \end{bmatrix}^{-1} [D_{m'}] [u_{xyz}^{sca}], \\
\sigma_{rz}^{scat} &= \sum_{m'=-M}^M \begin{bmatrix} E_{rz}^{m'}(\theta, z) \\ B_{m'} \end{bmatrix} \begin{bmatrix} A_{m'} \\ B_{m'} \end{bmatrix} = \sum_{m'=-M}^M \begin{bmatrix} E_{rz}^{m'}(\theta, z) \\ B_{m'} \end{bmatrix} \begin{bmatrix} \bar{A}B_{m'} \\ \bar{B} \end{bmatrix}^{-1} [D_{m'}] [u_{xyz}^{sca}].
\end{aligned} \tag{46}$$

where

$$\begin{aligned}
\begin{bmatrix} E_{rr}^{m'} \\ E_{r\theta}^{m'} \\ E_{rz}^{m'} \end{bmatrix} &= \begin{bmatrix} E_{rrA}^{m'0} & E_{rrA}^{m'1} & \dots & E_{rrA}^{m'n} & E_{rrB}^{m'0} & E_{rrB}^{m'2} & \dots & E_{rrB}^{m'n} \\ E_{r\theta A}^{m'0} & E_{r\theta A}^{m'1} & \dots & E_{r\theta A}^{m'n} & E_{r\theta B}^{m'0} & E_{r\theta B}^{m'2} & \dots & E_{r\theta B}^{m'n} \\ E_{rzA}^{m'0} & E_{rzA}^{m'1} & \dots & E_{rzA}^{m'n} & 0 & E_{rzB}^{m'2} & \dots & E_{rzB}^{m'n} \end{bmatrix}, \\
\begin{bmatrix} E_{rr}^{m'} \\ E_{r\theta}^{m'} \\ E_{rz}^{m'} \end{bmatrix} &= \begin{bmatrix} E_{rrA}^{m'0} & E_{rrA}^{m'1} & \dots & E_{rrA}^{m'n} & E_{rrB}^{m'0} & E_{rrB}^{m'2} & \dots & E_{rrB}^{m'n} \\ E_{r\theta A}^{m'0} & E_{r\theta A}^{m'1} & \dots & E_{r\theta A}^{m'n} & E_{r\theta B}^{m'0} & E_{r\theta B}^{m'2} & \dots & E_{r\theta B}^{m'n} \\ E_{rzA}^{m'0} & E_{rzA}^{m'1} & \dots & E_{rzA}^{m'n} & 0 & E_{rzB}^{m'2} & \dots & E_{rzB}^{m'n} \end{bmatrix}, \\
E_{rrA}^{mn} &= \left[\Sigma_{rr}^n(z) H_m(k_n a) - \tilde{\Sigma}_{rr}^n(z) \left(\frac{1}{a} H'_m(k_n a) - \frac{m^2}{k_n a^2} H_m(k_n a) \right) \right] e^{im\theta}, \\
E_{rrB}^{mn} &= im\mu \cos\left(\frac{n\pi z}{2h}\right) \left(\frac{2}{a} H'_m(l_n a) - \frac{2}{l_n a^2} H_m(l_n a) \right) e^{im\theta}, \\
E_{r\theta A}^{mn} &= im \Sigma_{r\theta}^n(z) \left(\frac{1}{a} H'_m(k_n a) - \frac{1}{k_n a^2} H_m(k_n a) \right) e^{im\theta}, \\
E_{r\theta B}^{mn} &= \mu \cos\left(\frac{n\pi z}{2h}\right) \left[\frac{2}{a} H'_m(l_n a) + \left(l_n - \frac{2m^2}{l_n a^2} \right) H_m(l_n a) \right] e^{im\theta}, \\
E_{rzA}^{mn} &= -\Sigma_{rz}^n(z) H'_m(k_n a) e^{im\theta}, \\
E_{rzB}^{mn} &= -im\mu \frac{n\pi}{2h} \sin\left(\frac{n\pi z}{2h}\right) \frac{1}{l_n a} H_m(l_n a) e^{im\theta}.
\end{aligned} \tag{47}$$

Therefore, the equivalent nodal forces at the virtual boundary can be denoted as

$$\begin{aligned}
F_x^{sca} &= \int_S N_J T_x^{sca} dS = \int_S N_J (\sigma_r^{sca} \cos\theta - \tau_{r\theta}^{sca} \sin\theta) dS \\
&= \int_S N_J \left\{ \sum_{m'=-M}^M \left(\begin{bmatrix} E_{rr}^{m'}(\theta, z) \\ B_{m'} \end{bmatrix} \begin{bmatrix} A_{m'} \\ B_{m'} \end{bmatrix} \right) \cos\theta - \sum_{m'=-M}^M \left(\begin{bmatrix} E_{r\theta}^{m'}(\theta, z) \\ B_{m'} \end{bmatrix} \begin{bmatrix} A_{m'} \\ B_{m'} \end{bmatrix} \right) \sin\theta \right\} dS \\
&= \int_S N_J \left\{ \sum_{m'=-M}^M \left(\begin{bmatrix} E_{rr}^{m'}(\theta, z) \\ B_{m'} \end{bmatrix} \begin{bmatrix} \bar{A}B_{m'} \\ \bar{B} \end{bmatrix}^{-1} [D_{m'}] [u_{xyz}^{sca}] \right) \cos\theta \right. \\
&\quad \left. - \sum_{m'=-M}^M \left(\begin{bmatrix} E_{r\theta}^{m'}(\theta, z) \\ B_{m'} \end{bmatrix} \begin{bmatrix} \bar{A}B_{m'} \\ \bar{B} \end{bmatrix}^{-1} [D_{m'}] [u_{xyz}^{sca}] \right) \sin\theta \right\} dS,
\end{aligned} \tag{49}$$

$$\begin{aligned}
F_y^{\text{sca}} &= \int_S N_J T_y^{\text{sca}} dS = \int_S N_J (\sigma_r^{\text{sca}} \sin \theta + \tau_{r\theta}^{\text{sca}} \cos \theta) dS \\
&= \int_S N_J \left\{ \sum_{m'=-M}^M \left([E_{rr}^{m'}(\theta, z)] \begin{bmatrix} A_{m'} \\ B_{m'} \end{bmatrix} \right) \sin \theta + \sum_{m'=-M}^M \left([E_{r\theta}^{m'}(\theta, z)] \begin{bmatrix} A_{m'} \\ B_{m'} \end{bmatrix} \right) \cos \theta \right\} dS \\
&= \int_S N_J \left\{ \sum_{m'=-M}^M \left([E_{rr}^{m'}(\theta, z)] [\bar{A}B_{m'}]^{-1} [D_{m'}] [u_{xyz}^{\text{sca}}] \right) \sin \theta \right. \\
&\quad \left. + \sum_{m'=-M}^M \left([E_{r\theta}^{m'}(\theta, z)] [\bar{A}B_{m'}]^{-1} [D_{m'}] [u_{xyz}^{\text{sca}}] \right) \cos \theta \right\} dS,
\end{aligned} \tag{50}$$

$$\begin{aligned}
F_z^{\text{sca}} &= \int_S N_J T_z^{\text{sca}} dS = \int_S N_J \tau_{rz}^{\text{sca}} dS \\
&= \int_S N_J \sum_{m'=-M}^M \left([E_{rz}^{m'}(\theta, z)] \begin{bmatrix} A_{m'} \\ B_{m'} \end{bmatrix} \right) dS \\
&= \int_S N_J \sum_{m'=-M}^M \left([E_{rz}^{m'}(\theta, z)] [\bar{A}B_{m'}]^{-1} [D_{m'}] [u_{xyz}^{\text{sca}}] \right) dS.
\end{aligned} \tag{51}$$

Projecting the integral value on the local node J in Eq.49, Eq.50 and Eq.51 onto the global node p , we get

$$\begin{aligned}
\int_S N_J \left([E_{rr}^{m'}(\theta, z)] \cos \theta - [E_{r\theta}^{m'}(\theta, z)] \sin \theta \right) dS &\rightarrow [G_{m'}^{x_p}] \\
\int_S N_J \left([E_{rr}^{m'}(\theta, z)] \sin \theta + [E_{r\theta}^{m'}(\theta, z)] \cos \theta \right) dS &\rightarrow [G_{m'}^{y_p}] \\
\int_S N_J [E_{rz}^{m'}(\theta, z)] dS &\rightarrow [G_{m'}^{z_p}]
\end{aligned} \tag{52}$$

Finally, the equivalent nodal force matrix can be expressed as

$$[F_{xyz}^{\text{sca}}]_{3p \times 1} = \begin{bmatrix} \bar{F}^{\text{sca}} \end{bmatrix}_{3p \times 3p} \cdot [u_{xyz}^{\text{sca}}]_{3p \times 1} \tag{53}$$

where

$$\begin{bmatrix} \bar{F}^{\text{sca}} \end{bmatrix}_{3p \times 3p} = \sum_{m'=-M}^M [G_{m'}]_{3p \times (\frac{3}{2}N+2)} \begin{bmatrix} \bar{A}B_{m'} \end{bmatrix}_{(\frac{3}{2}N+2) \times (\frac{3}{2}N+2)}^{-1} [D_{m'}]_{(\frac{3}{2}N+2) \times 3p} \tag{54}$$

$$[G_{m'}]_{3p \times (\frac{3}{2}N+2)} = \begin{bmatrix} G_{m'}^{x_1} \\ G_{m'}^{y_1} \\ G_{m'}^{z_1} \\ \vdots \\ G_{m'}^{x_p} \\ G_{m'}^{y_p} \\ G_{m'}^{z_p} \end{bmatrix} \quad (55)$$

2.4. Three-dimensional DtN-FEM formulation

The elasto-dynamic finite element formulation is

$$([K] - \omega^2 [M]) [U^{\text{tot}}] = [F^{\text{tot}}] \quad (56)$$

where ω is the angular frequency, and

$$\begin{aligned} [K] &= \int_S [B]^T [D] [B] dS, & [M] &= \rho \int_S [N]^T [N] dS, \\ [U^{\text{tot}}] &= [U^{\text{inc}}] + [U^{\text{sca}}], & [F^{\text{tot}}] &= [F^{\text{inc}}] + [F^{\text{sca}}]. \end{aligned} \quad (57)$$

and $[N]$ is the matrix of shape function, $[B]$ is the geometric matrix, $[D]$ is the elastic matrix, $[K]$ is the stiffness matrix, $[M]$ is the mass matrix, and ρ is the material density.

Utilizing Eq.53, Eq.56 can be finally simplified as

$$[U^{\text{sca}}] = \{ ([K] - \omega^2 [M]) - [\bar{F}^{\text{sca}}] \}^{-1} \{ [F^{\text{inc}}] - ([K] - \omega^2 [M]) [U^{\text{inc}}] \} \quad (58)$$

which is the basic DtN-FEM formulation.

3. Numerical examples

In this section, the validity will be presented in order to verify the correctness and efficiency of our proposed DtN-FEM. Here, the DtN-FEM results will be compared with the BEM results. Furthermore, parametric analysis about the effect on different defect shapes will be discussed detailedly.

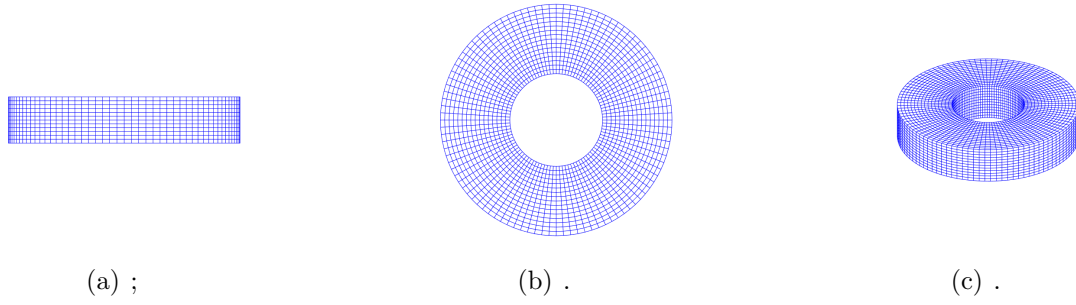


Figure 2: aa

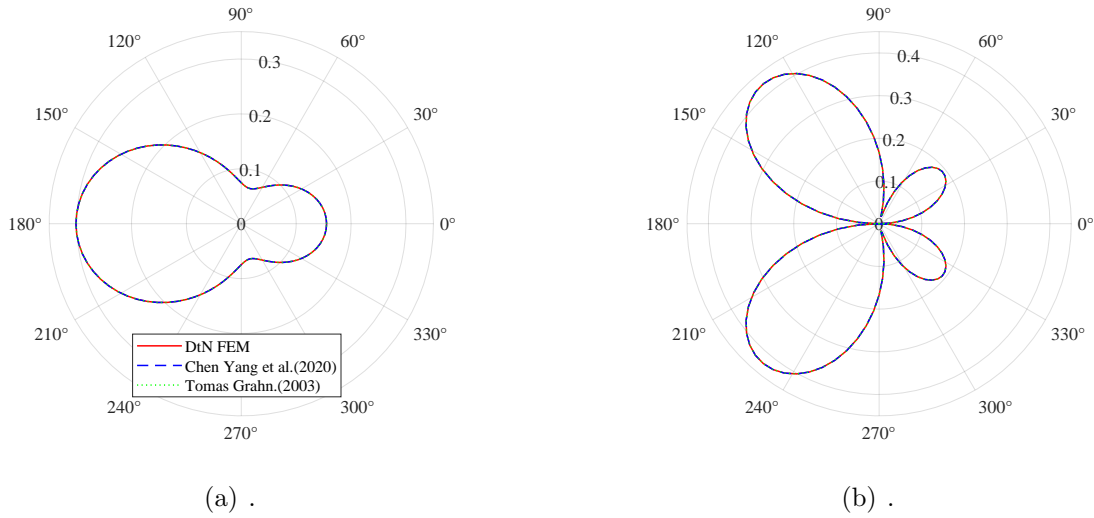


Figure 3: Error analysis of energy balance

4. Conclusion

This paper proposed a three-dimensional DtN FEM to analyze the scattering of Lamb and SH guided waves due to different shapes in an infinite 3D plate. This method is simple and elegant, which has advantages on dimension reduction and needs no absorption medium or perfectly matched layer to suppress the reflected waves compared to traditional FEM. For the future development, the scattering data from forward analysis by proposed 3D DtN FEM will subsequently be used for the inverse analysis of reconstructing both the location and shape of 3D defects.

5. Conflicts of Interest

The authors declare that they have no known competing financial interests or personal relationships that could have appeared to influence the work reported in this paper.

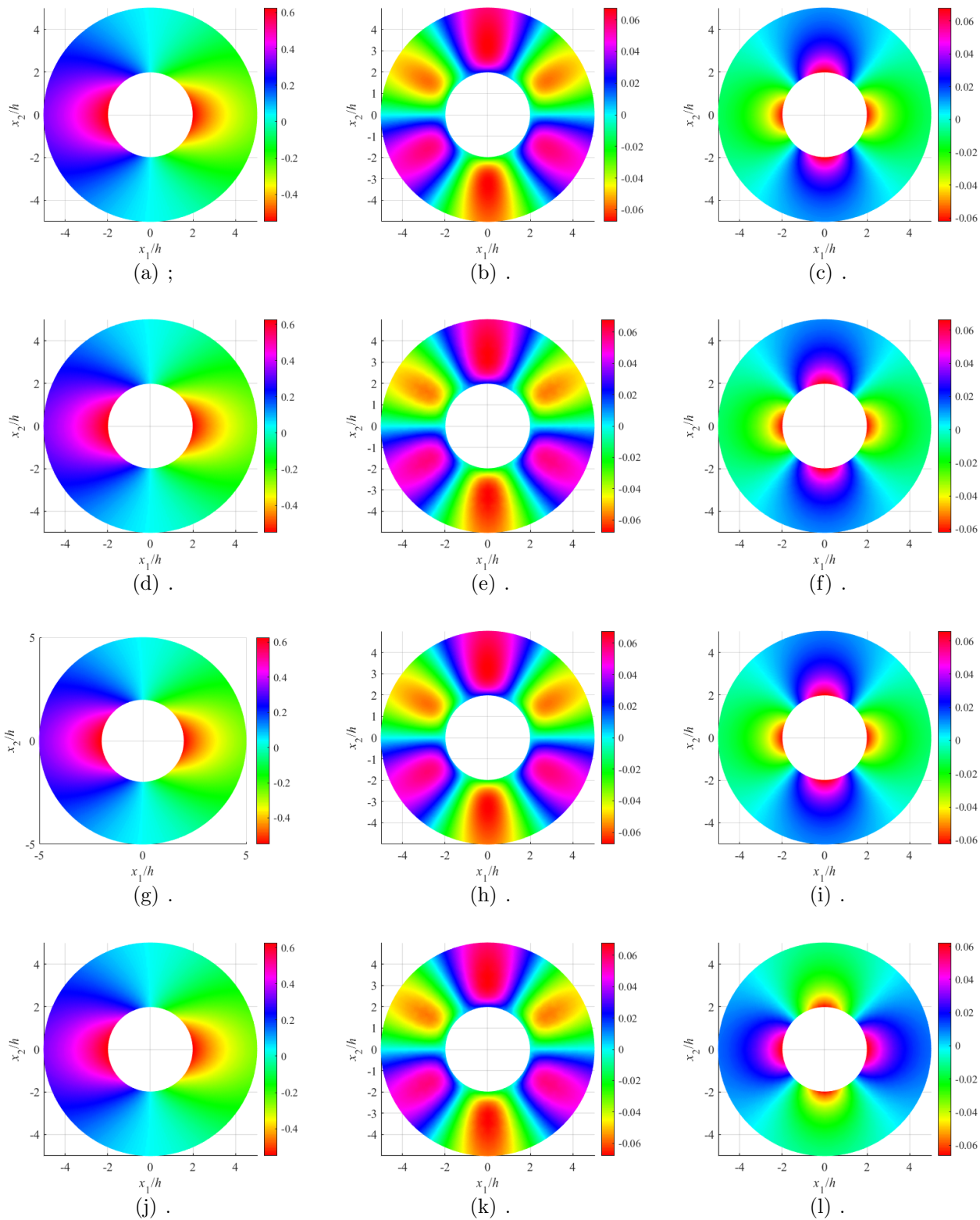


Figure 4: aa

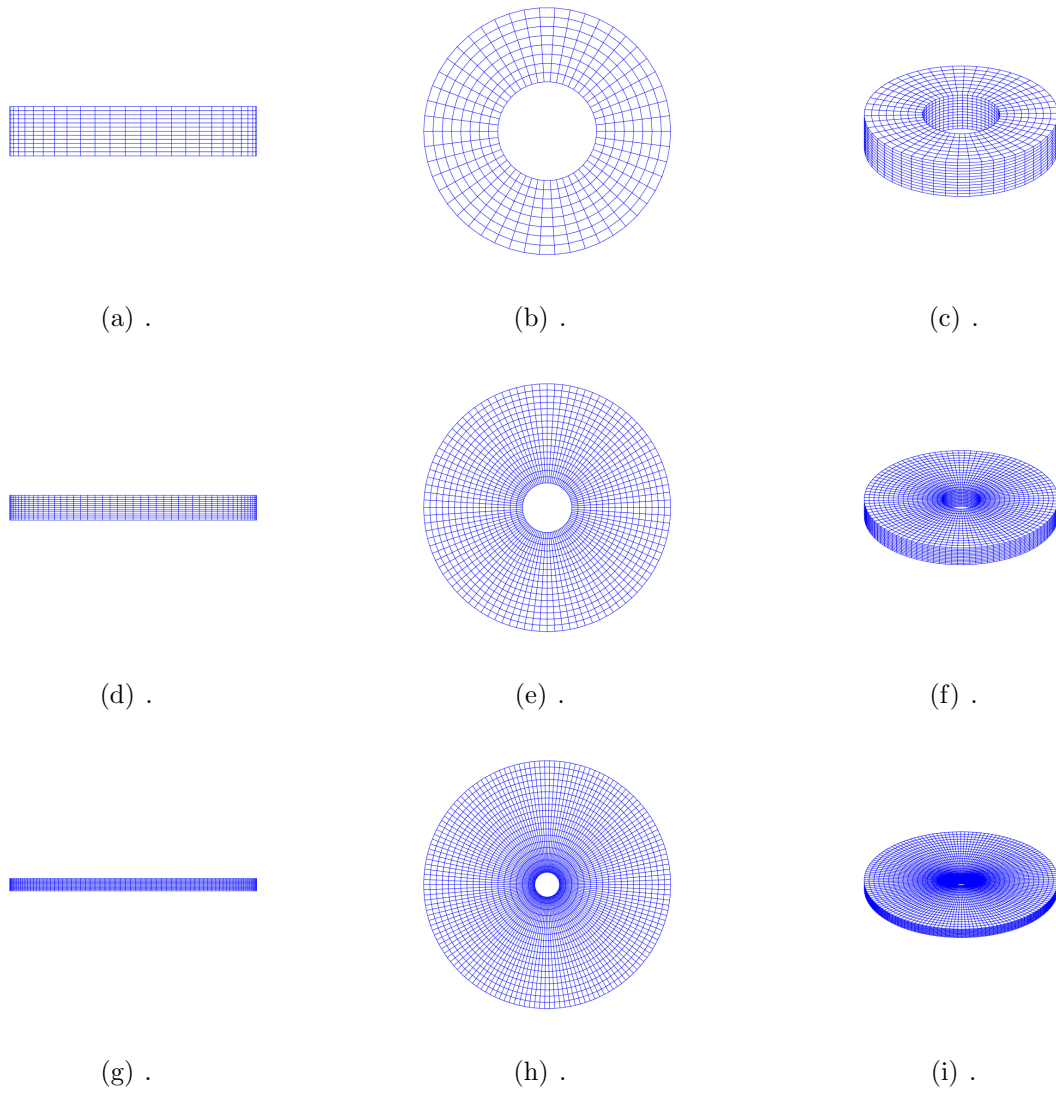


Figure 5: Error analysis of energy balance

Acknowledgments

This work was supported by the National Natural Science Foundation of China (Grant No. 12402098), the China Scholarships Council (Grant No. 202106830041) and the Fundamental Research Funds for the Central Universities (Grant No. 7100604733).

References

- [1] Y. Da, B. Wang, D. Liu, Z. Qian, An analytical approach to reconstruction of axisymmetric defects in pipelines using $t(0, 1)$ guided waves, *Applied Mathematics and Mechanics* (English Edition) 41 (10) (2020) 1479–1492.

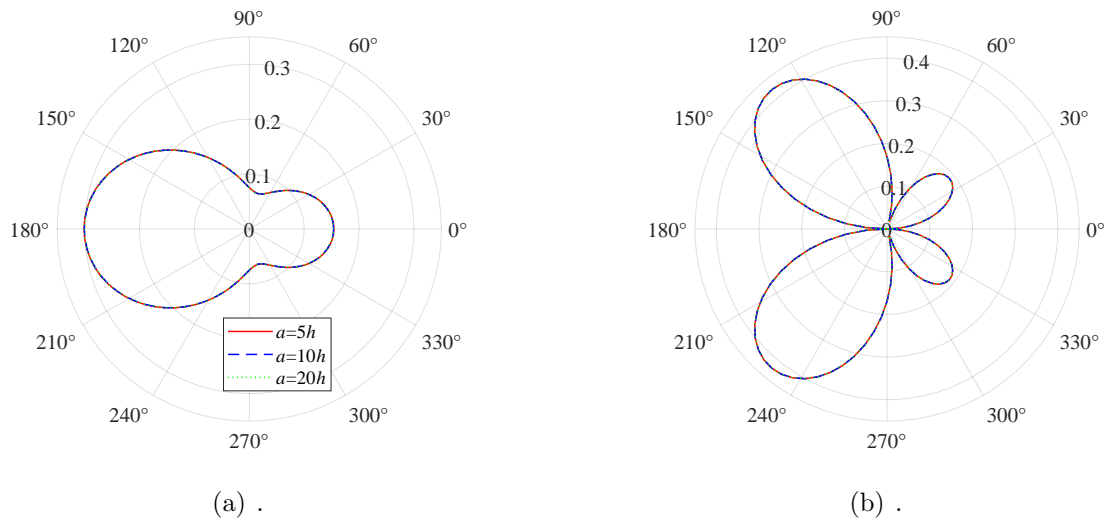


Figure 6: Error analysis of energy balance

- [2] Y. Da, G. Dong, Y. Shang, B. Wang, D. Liu, Z. Qian, Circumferential defect detection using ultrasonic guided waves: An efficient quantitative technique for pipeline inspection, *Engineering Computations (Swansea, Wales)* 37 (6) (2020) 1923–1943.
- [3] B. Wang, S. Hirose, Inverse problem for shape reconstruction of plate-thinning by guided sh-waves, *Materials Transactions* 53 (10) (2012) 1782–1789.
- [4] B. Wang, Z. Qian, S. Hirose, Inverse shape reconstruction of inner cavities using guided sh-waves in a plate, *Shock and Vibration* 2015.
- [5] B. Wang, Y. Da, Z. Qian, Forward and inverse studies on scattering of rayleigh wave at surface flaws, *Applied Sciences (Switzerland)* 8 (3).
- [6] B. Wang, C. Yang, Z. Qian, Forward and inverse analysis of love wave scattering by interface cavities, *Journal of Theoretical and Computational Acoustics* 27 (3).
- [7] Y. Da, G. Dong, B. Wang, D. Liu, Z. Qian, A novel approach to surface defect detection, *International Journal of Engineering Science* 133 (2018) 181–195.
- [8] C. Yang, B. Wang, Z. Qian, Forward analysis of love-wave scattering due to a cavity-like defect, *Shock and Vibration* 2018.
- [9] C. Yang, B. Wang, Z. Qian, Three dimensional modified bem analysis of forward scattering problems in elastic solids, *Engineering Analysis with Boundary Elements* 122 (2021) 145–154.

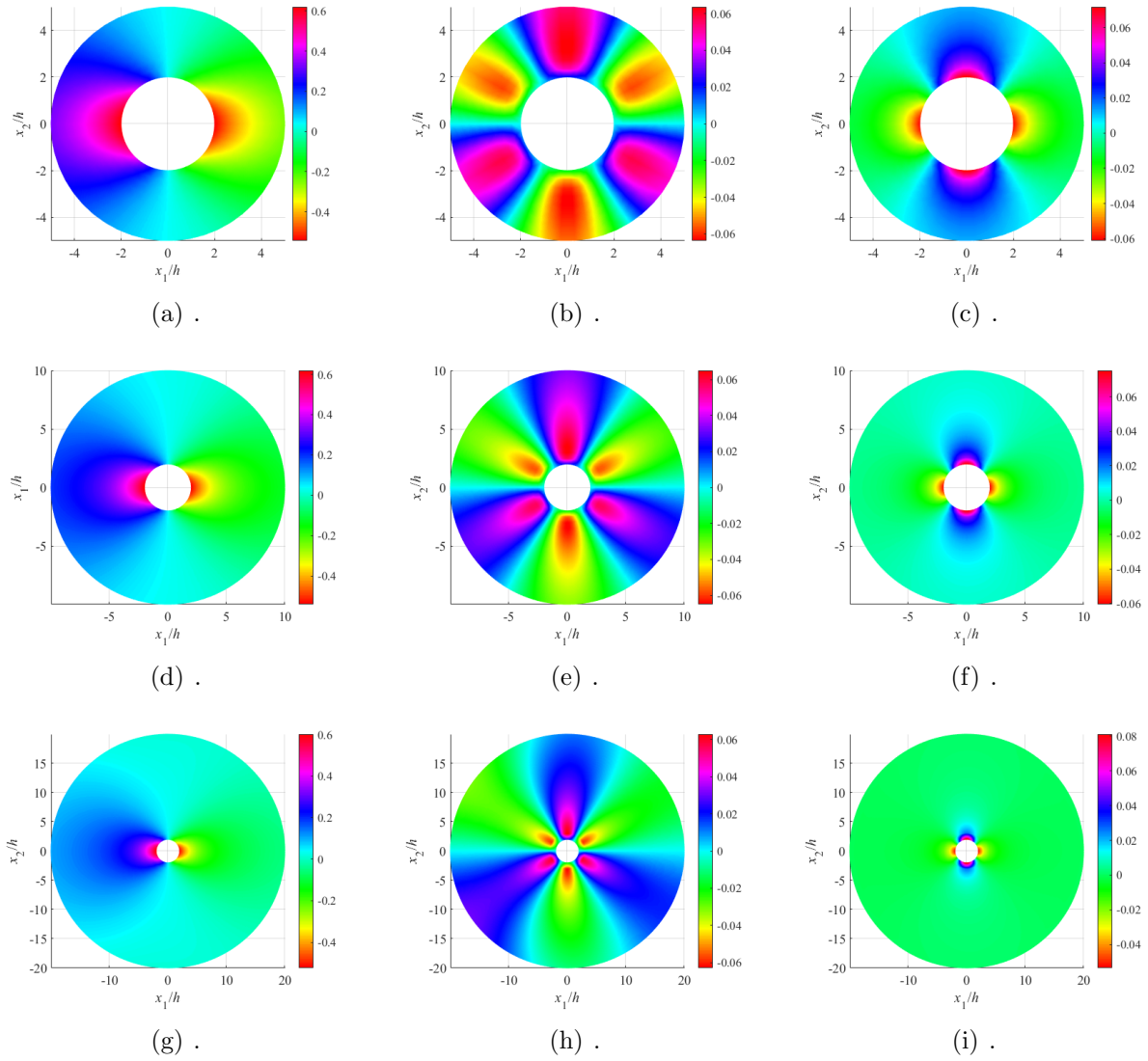


Figure 7: Error analysis of energy balance

- [10] M. Koshiba, S. Karakida, M. Suzuki, Finite-element analysis of lamb wave scattering in an elastic plate waveguide, *IEEE Transactions on Sonics and Ultrasonics* 31 (1) (1984) 18–24.
- [11] Y. Al-Nassar, S. Datta, A. Shah, Scattering of lamb waves by a normal rectangular strip weldment, *Ultrasonics* 29 (2) (1991) 125–132.
- [12] T. Hayashi, J. Rose, Guided wave simulation and visualization by a semianalytical finite element method, *Materials Evaluation* 61 (1) (2003) 75–79.
- [13] D. Ramatlo, C. Long, P. Loveday, D. Wilke, A modelling framework for simulation of ultrasonic guided wave-based inspection of welded rail tracks, *Ultrasonics* 108.

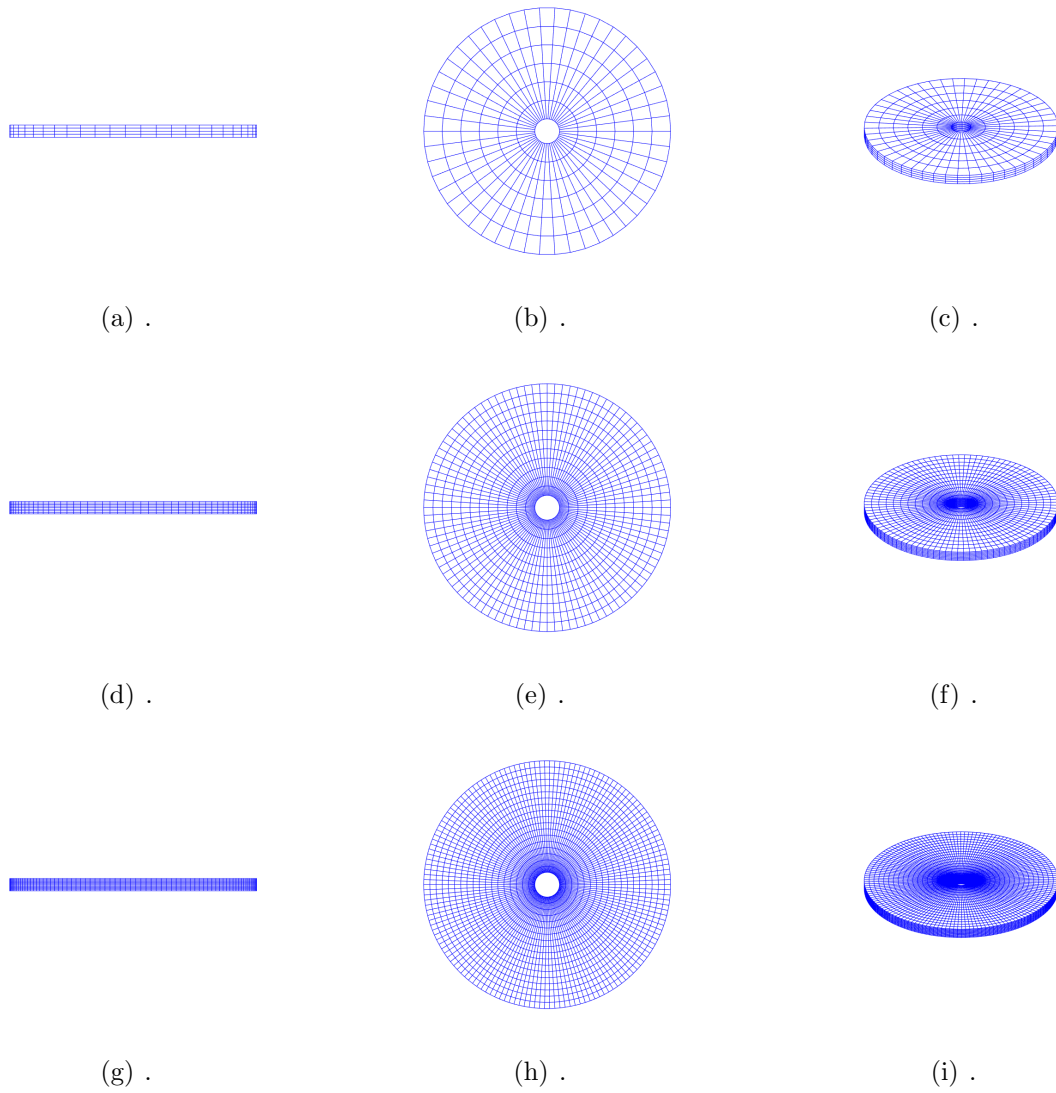


Figure 8: Error analysis of energy balance

- [14] G. Yue, X. Cui, K. Zhang, Z. Wang, D. An, Guided wave propagation for monitoring the rail base, *Mathematical Problems in Engineering* 2020.
- [15] A. Gunawan, S. Hirose, Mode-exciting method for lamb wave-scattering analysis, *Journal of the Acoustical Society of America* 115 (3) (2004) 996–1005.
- [16] G. Shkerdin, C. Glorieux, Lamb mode conversion in a plate with a delamination, *Journal of the Acoustical Society of America* 116 (4 I) (2004) 2089–2100.
- [17] L. Moreau, M. Castaings, B. Hosten, M. Predoi, An orthogonality relation-based technique for post-processing finite element predictions of waves scattering in solid waveguides, *Journal of the Acoustical Society of America* 120 (2) (2006) 611–620.

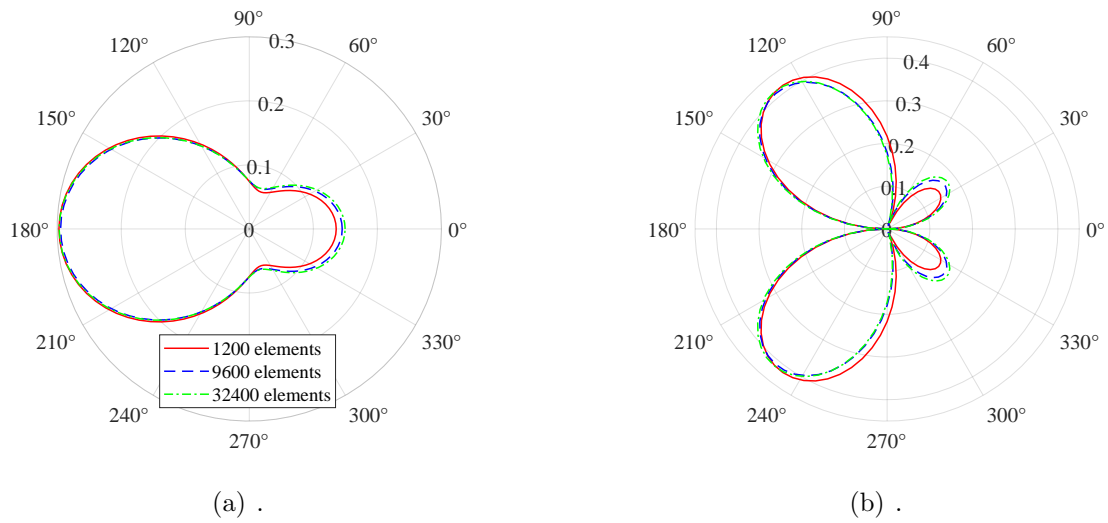


Figure 9: Error analysis of energy balance

- [18] A. Kubrusly, J. von der Weid, S. Dixon, Experimental and numerical investigation of the interaction of the first four sh guided wave modes with symmetric and non-symmetric discontinuities in plates, *NDT and E International* 108.
- [19] A. Kubrusly, P. Tovar, J. von der Weid, S. Dixon, Mode conversion of sh guided waves with symmetry inversion in plates, *Ultrasonics* 112.

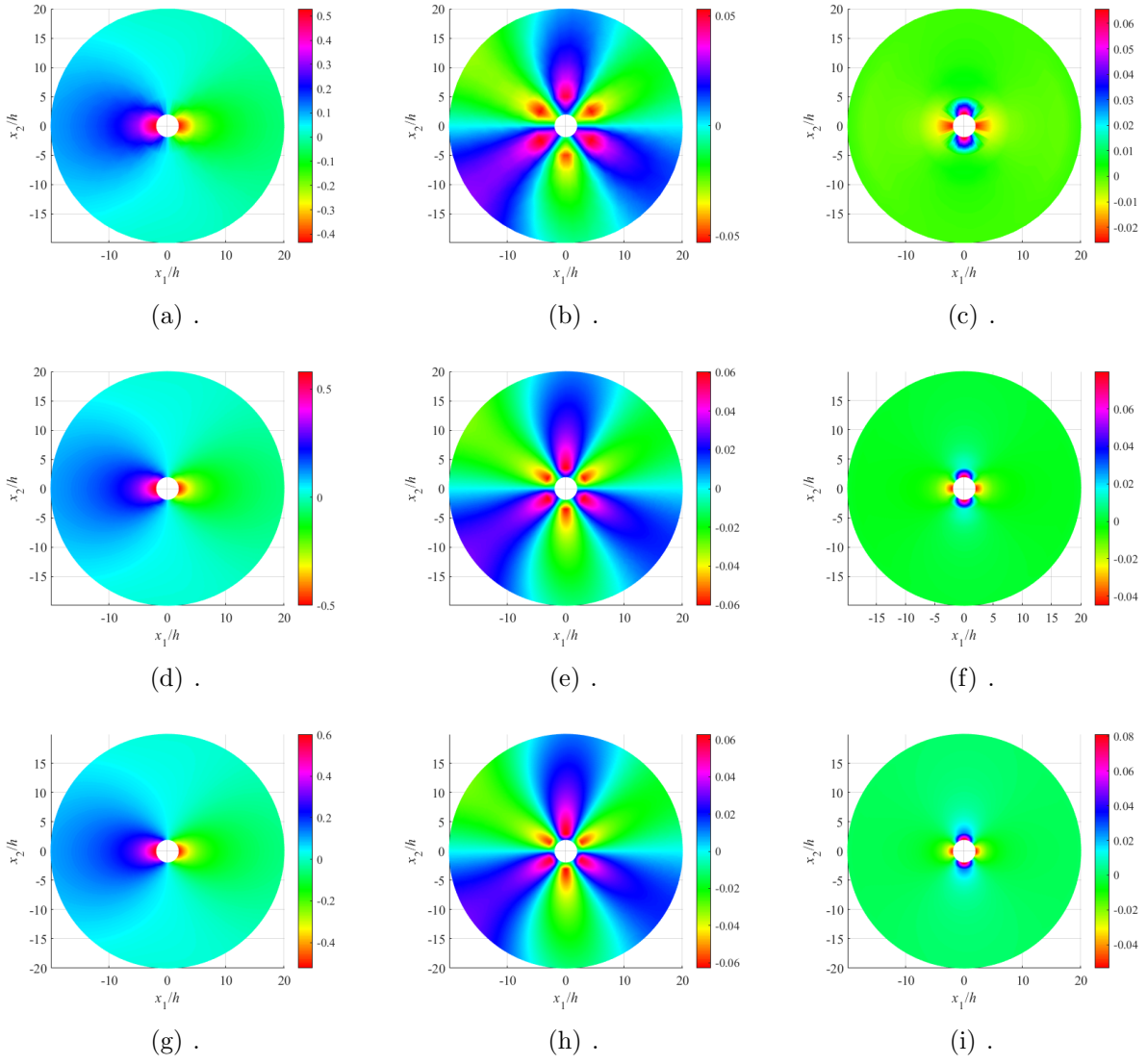


Figure 10: Error analysis of energy balance

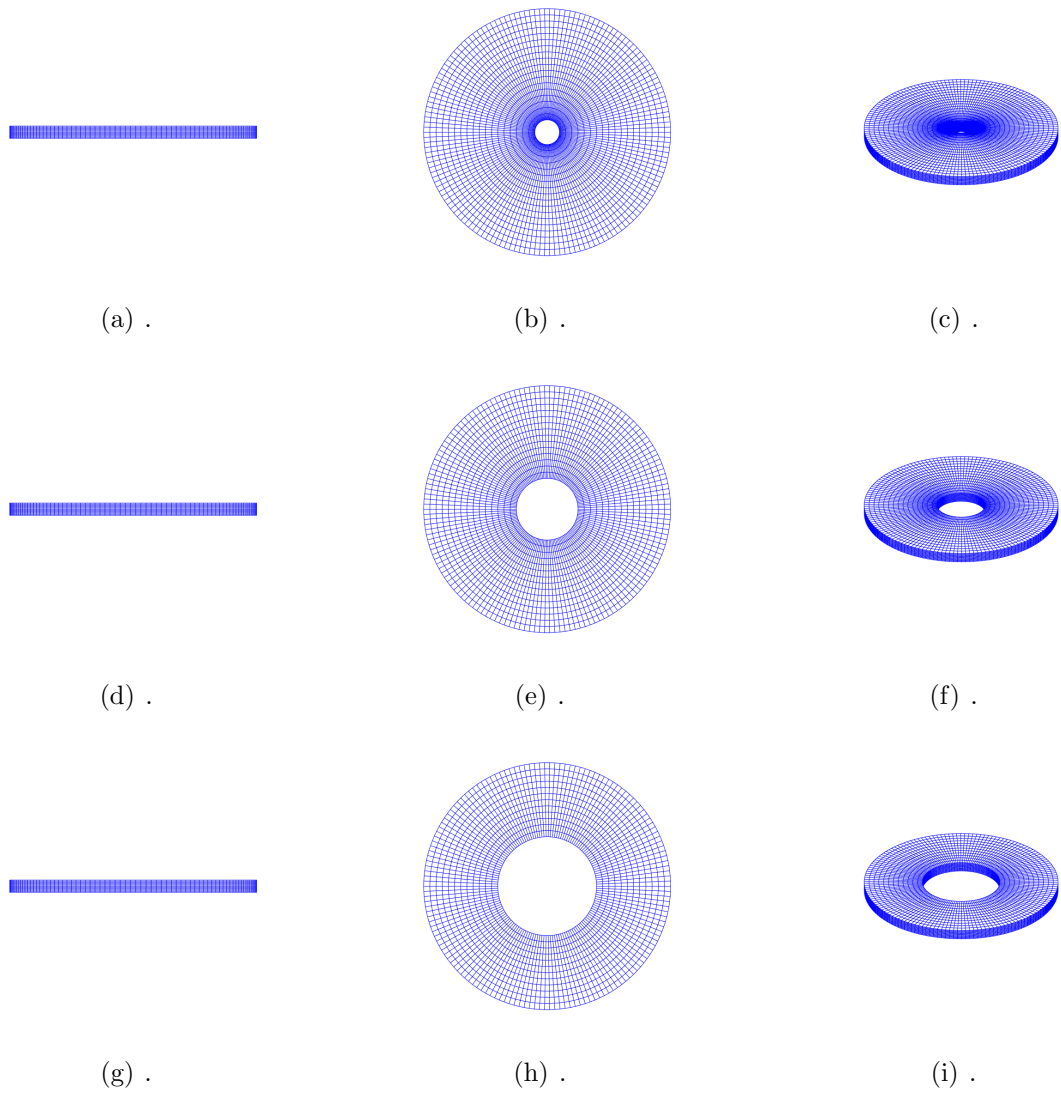


Figure 11: Error analysis of energy balance

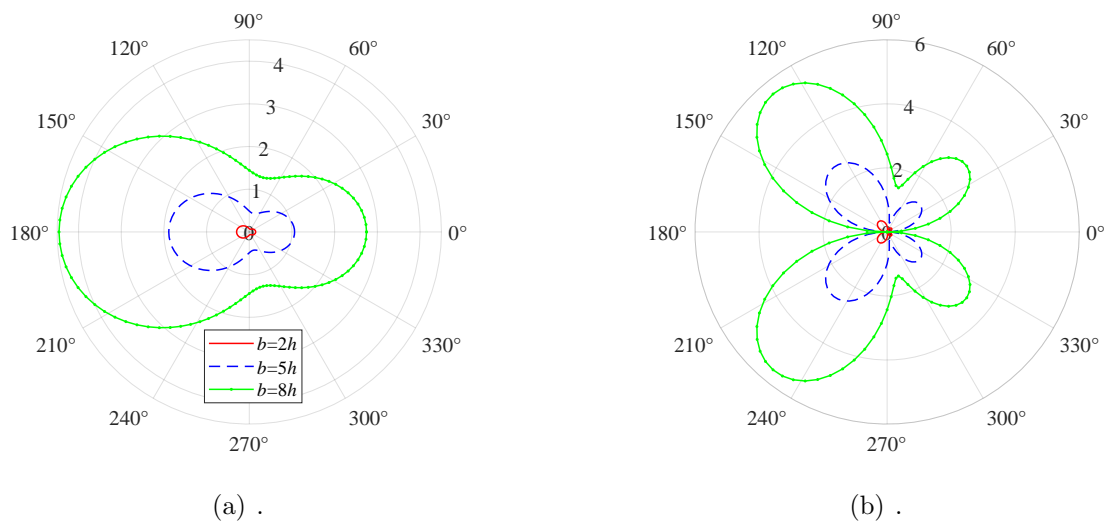


Figure 12: Error analysis of energy balance

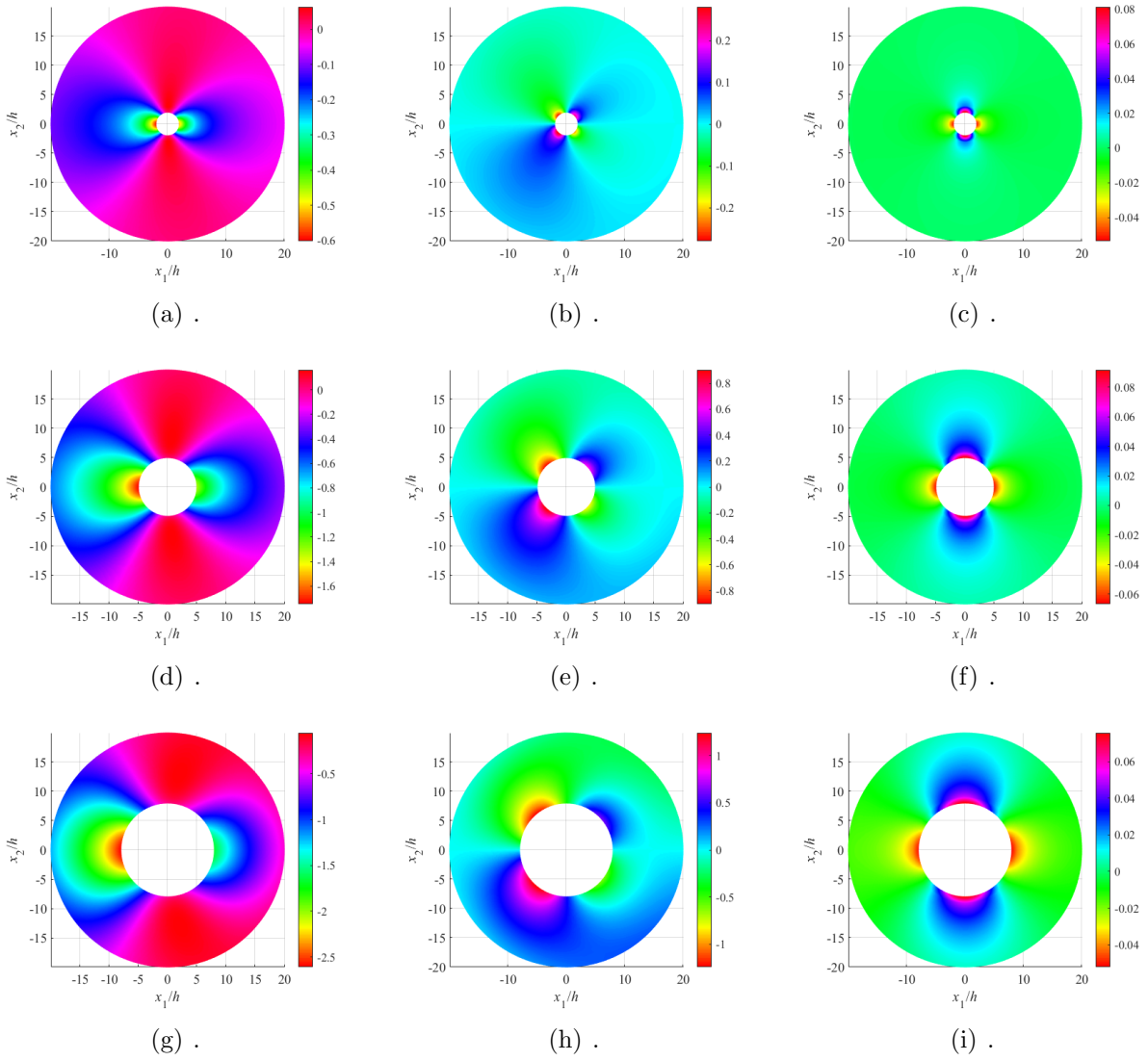


Figure 13: Error analysis of energy balance

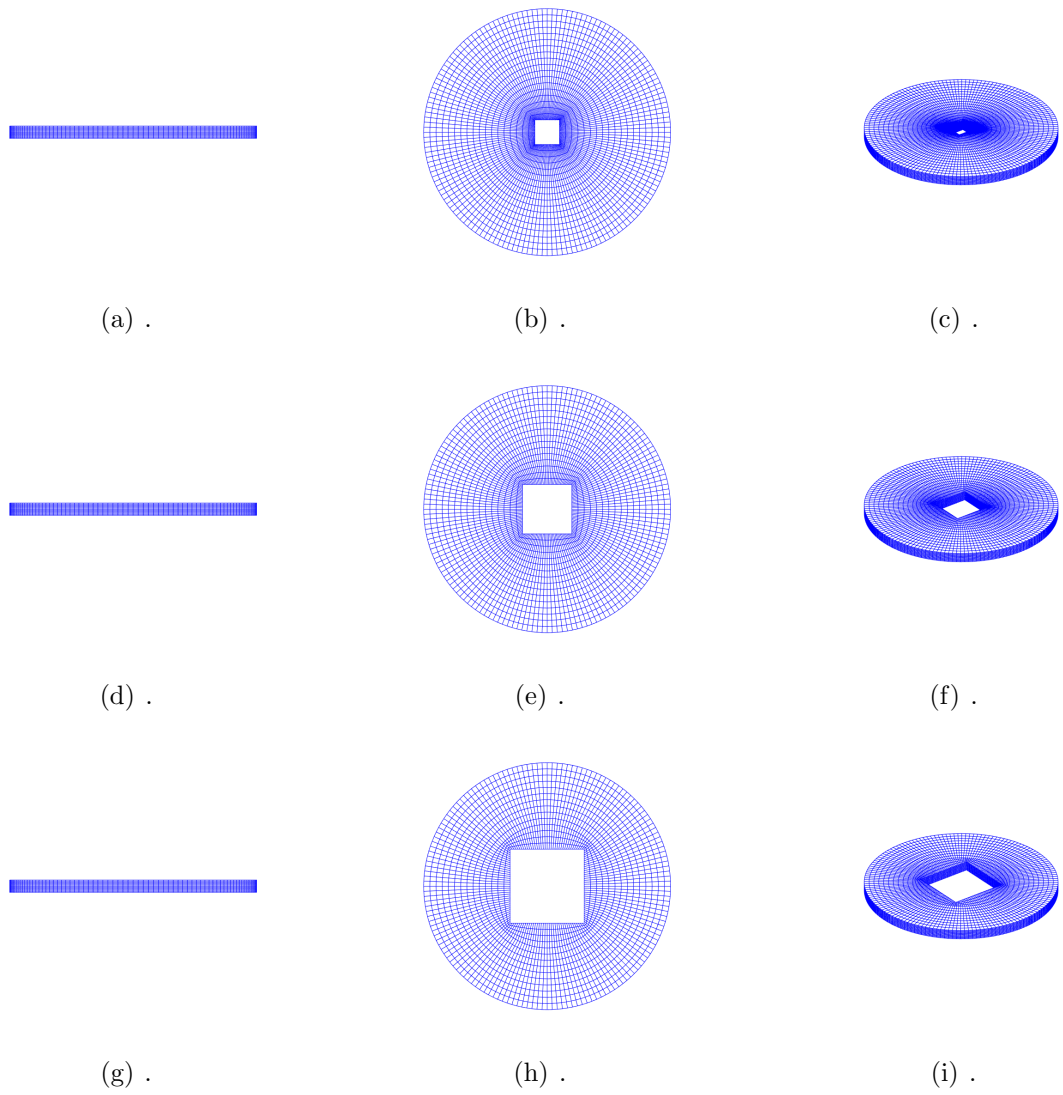


Figure 14: Error analysis of energy balance

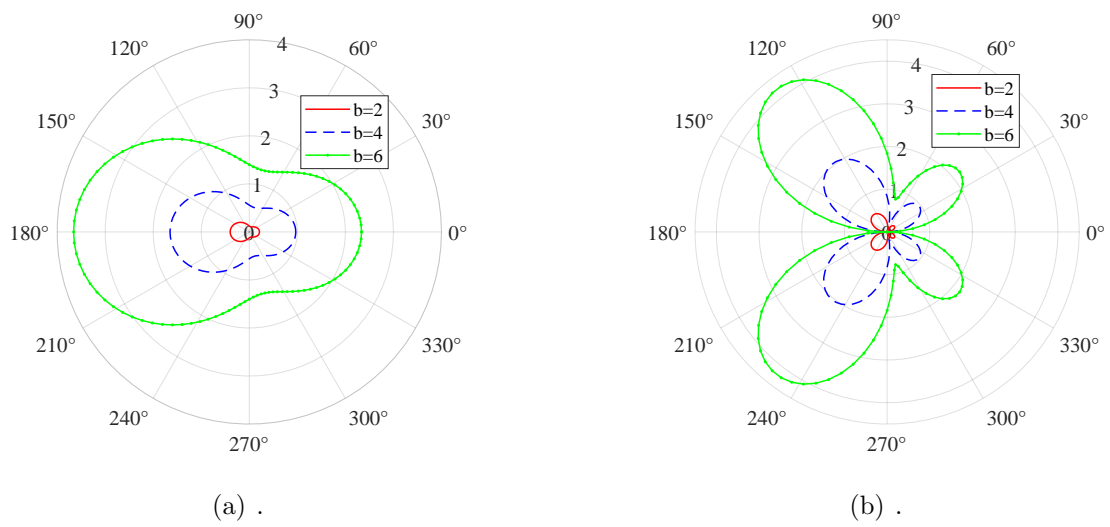


Figure 15: Error analysis of energy balance

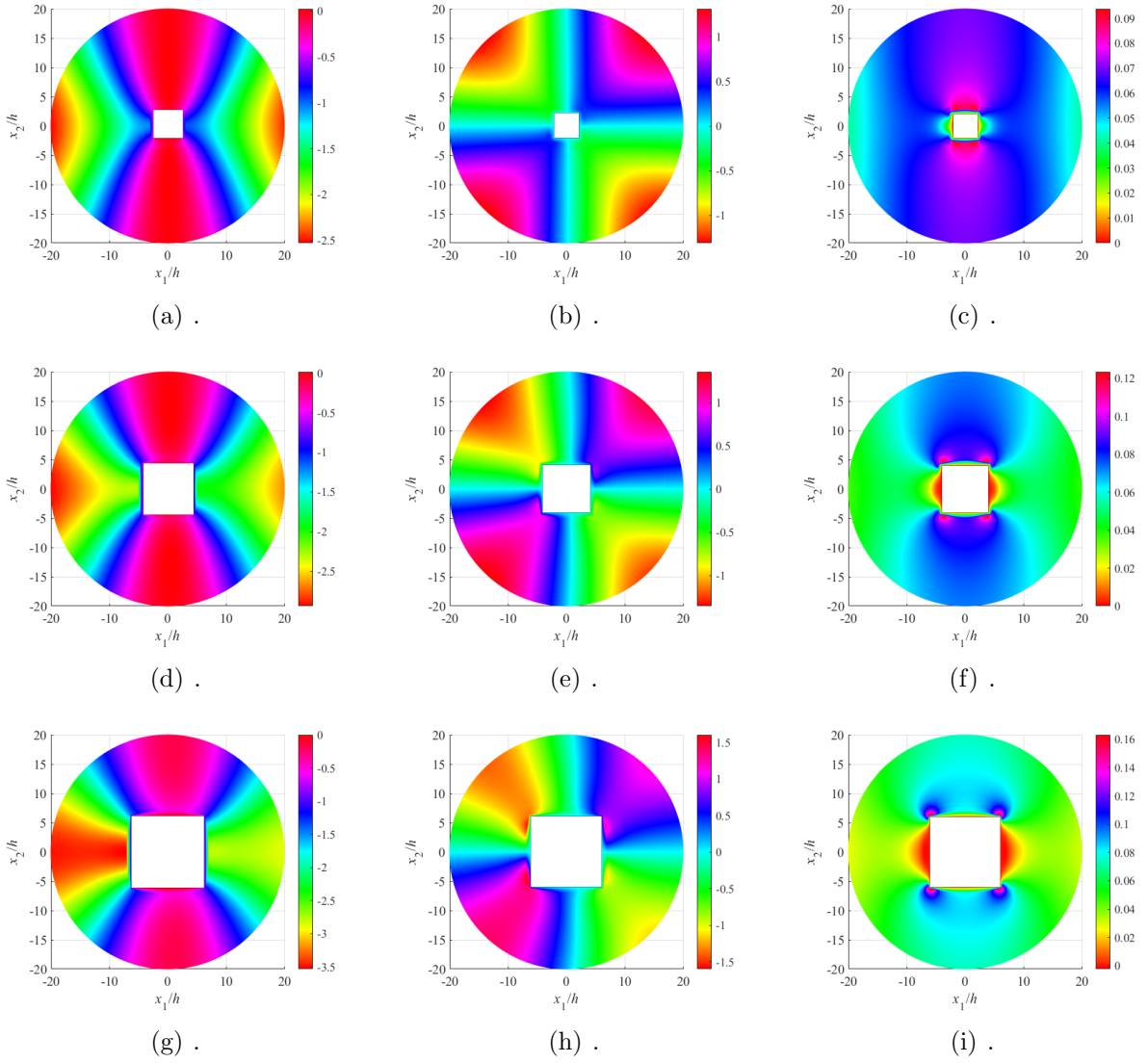


Figure 16: Error analysis of energy balance